Downloaded from orbit.dtu.dk on: May 06, 2023

DTU Library

A “poor man's approach” to topology optimization of cooling channels based on a Darcy flow model

Zhao, Xi; Zhou, Mingdong; Sigmund, Ole; Andreasen, Casper Schousboe

Published in:
International Journal of Heat and Mass Transfer

Link to article, DOI:
10.1016/j.ijheatmasstransfer.2017.09.090

Publication date:
2018

Document Version
Peer reviewed version

Link back to DTU Orbit

Citation (APA):
Zhao, X., Zhou, M., Sigmund, O., & Andreasen, C. S. (2018). A “poor man's approach” to topology optimization of cooling channels based on a Darcy flow model. *International Journal of Heat and Mass Transfer*, *116*, 1108-1123. https://doi.org/10.1016/j.ijheatmasstransfer.2017.09.090

General rights
Copyright and moral rights for the publications made accessible in the public portal are retained by the authors and/or other copyright owners and it is a condition of accessing publications that users recognise and abide by the legal requirements associated with these rights.

- Users may download and print one copy of any publication from the public portal for the purpose of private study or research.
- You may not further distribute the material or use it for any profit-making activity or commercial gain
- You may freely distribute the URL identifying the publication in the public portal

If you believe that this document breaches copyright please contact us providing details, and we will remove access to the work immediately and investigate your claim.

A "poor man's approach" to topology optimization of cooling channels based on a Darcy flow model

Xi Zhao[a,1], Mingdong Zhou ✉[b,2], Ole Sigmund[c,3], Casper Schousboe Andreasen[c,4]

[a]*School of Automobile Engineering, Dalian University of Technology*
No.2 Ligong Road Dalian China
[b]*State Key Laboratory of Mechanical System and Vibration*
Shanghai Key Laboratory of Digital Manufacture for Thin-walled Structures
Shanghai Jiao Tong University, No. 800 Dong Chuan Rd. Shanghai 200240, P.R. China
[c]*Department of Mechanical Engineering, Technical University of Denmark*
Building 404, Nils Koppels Allé, 2800 Kgs. Lyngby, Denmark

Abstract

A topology optimization methodology for optimizing cooling channels using an approximate but low-cost flow and heat transfer model is presented. The fluid flow is modeled using the Darcy model, which is a linear problem that can be solved very efficiently compared to the Navier-Stokes equations. The obtained fluid velocity is subsequently used in a stabilized convection-diffusion heat transfer model to calculate the temperature distribution. The governing equations are cast in a monolithic form such that both the solid and fluid can be modeled using a single equation set. The material properties: permeability, conductivity, density and specific heat capacity are interpolated using the Solid Isotropic Material with Penalization (SIMP) scheme. Manufacturable cooling-channel designs with clear topologies are obtained with the help of a pressure drop constraint and a geometric length-scale constraint. Several numerical examples demonstrate the applicability of this approach. Verification studies with a full turbulence model show that, although the equivalent model has limitations in yielding a perfect realistic velocity field, it generally provides well-performing cooling channel designs.

Keywords: Darcy flow, Convective heat transfer, Cooling channels, Topology optimization, length-scale control

1. Introduction

Many engineering products and processes such as engines, batteries and

[1]Xi Zhao email: zhaoxivipdlut@mail.dlut.edu.cn
[2]✉Mingdong Zhou email: mdzhou@sjtu.edu.cn
[3]Ole Sigmund email: sigmund@mek.dtu.dk
[4]Casper Schousboe Andreasen email: csan@mek.dtu.dk

CPUs are subject to heat loading from combustion processes or Joule heating. Other heat loads could be due to friction as in stamping or deep-drawing or come from hot solidifying material used in injection molding or direct heat conduction from the stamp in hot stamping processes. Most of this heat is harmful and it is important to transport this heat away from the working zone such that the final product complies with the tolerance requirements and to ensure a long lifetime of both product and tool. Besides this, the successful repeated and fast manufacturing of components also relies on the ability to control the local temperature of the process.

A standard method to remove heat is by letting a cooling liquid pass through channels in the heat generating component. A liquid cycling system would then transport the heat from the component to a heat exchanger. An effective cooling strategy depends on the distribution, periodicity and strength of potentially multiple heat sources. Amongst different processes, some may prefer a low temperature of the tool while others may benefit from a constant but higher temperature. Layout and shape of the cooling channels hence become crucial for the success of the manufacturing activities.

Much effort has already been invested by engineers and researchers in designing efficient cooling systems [9, 16, 22]. A typical optimization approach for cooling system design is by parametric optimization of channels in a predefined layout. Tan et al.[25] introduce a gradient-based cooling channel design methodology with parametrized geometric control points. Jarrett[17] uses the distance and thickness of channels as parameters to optimize heat transport in battery. Qiao[22] presents a 2D pipe section optimization design by using the boundary element method. Wang et al.[27] use a numerical experience based surrogate model for optimizing a 2D section design. Hu et al.[16] optimize a pipe design in a 3D model by taking the structural scale as parameters. Choi et al.[10] present a 3D channel design using a graphics pretreatment method to simplify the physical domain. However, such approaches do not allow introducing new channels or altering connectivity of channels during the optimization process.

The limitations of parametric optimization of cooling channels can be overcome by topology optimization[5], which is a systematic design approach for generating optimal material (here fluid) distributions. Originating from solid mechanics[4], this methodology has been extended to a wealth of other physical problems such as acoustics, electro-magnetics, heat transfer, fluid flow etc.

The general optimization of cooling channel systems involves flow simulation and convective heat transfer. Topology optimization was first applied to Stokes flow[6] and later extended to Navier-Stokes flow for low-to-moderate Reynolds numbers [12] by using a lubrication model approximation of flow between flat plates. An alternative interpolation model utilizing Darcy-Stokes flow was proposed by Guest[15] based on Brinkman's model[7] and Darcy's Law. In the lubrication approximation, a coefficient of viscous force is interpolated to control the flow. In the Darcy-Stokes model, the interpolation between solid and fluid is based on a porous flow assumption. The two models are related and they end up with similar structure where fluid flow in solid regions is penalized

by an artificial force term proportional to the local velocity. The method was further extended to transport problems[3] in the form of passive mixer design. In recent years, problems including both forced and natural convection have attracted much attention in the quest for optimizing cooling profiles and heat exchangers. Dede[11] used a Brinkman model to optimize the cooling profile of jet impingement surfaces. Heat-sink devices were designed using a Brinkman penalization applied to the Stokes model in [18]. Yoon[28] focused on the forced convection heat transfer problem using Navier-Stokes equations to describe the fluid field. Alexandersen et al.[1, 2] focused on cooling by natural convection in 2D and 3D problems. Zhou et al. [29] utilized a simpler engineering model for topology optimization of conductive and convective heat transfer problems. The latter uses the convective heat transfer coefficient to describe the convective thermal load and thus the overall system is solved very efficiently.

For practical cooling channel design, the most widely used simulation models are turbulent flow models coupled with convective heat transfer via the fluid velocity. Such complex models require non-linear solution schemes and boundary capturing meshing for simulation, which is time-consuming and thus unattractive for early stage conceptual design studies using topology optimization. Hence, there is demand for an efficient model to predict the fluid and temperature distributions using a computationally cheap but still sufficiently accurate method.

In this paper, a Darcy (potential) flow-based topology optimization approach is introduced for designing cooling channels. The temperature and heat transport is modeled using a stabilized convection-diffusion heat transfer model on top of the Darcy model. The modeling error between the Darcy and turbulent flow model is compared with the commercial software COMSOL. By parameter studies suitable relations between the material properties involved in the optimization process are found in order to minimize this error. The manufacturability of the resulting designs, i.e. clear black and white topology layouts with strongly enforced mimimum length scale, are ensured using a combined projection and geometric constraint approach (c.f. [23], [30]). The optimization problem is solved by the method of moving asymptotes (MMA)[24]. The optimized designs are verified with a complex thermo-fluidic model and show a similar trend in optimized performance but the accuracy of the temperature field cannot be guaranteed.

The remainder of the text is organized as follows. In section 2, the Darcy-flow based convective heat transfer model is introduced and compared with a turbulent flow based model. The material properties of the solid and fluid phases are also studied and equivalent parameters for the simplified model are obtained. In section 3.1, the material interpolation, filtering and projection methods are introduced. Topology optimization formulation and related constraints are discussed in section 3.2. Section 4 presents several numerical examples with associated discussion. Conclusions are given in section 5.

2. Physical model

Fig. 1 shows a generic cooling system design problem. The physical design domain Ω consists of a solid phase domain Ω_s, a water phase domain Ω_w as $\Omega = \Omega_s \cup \Omega_w$. The boundary of the domain Ω is divided into two parts, an outlet boundary Γ_1 and an inlet boundary Γ_2. Boundary conditions such as prescribed pressure, $p = p_0$ or prescribed velocity, $\mathbf{u} \cdot \mathbf{n} = \mathrm{u}_0$, can be applied on both inlet and outlet, where $\mathbf{n}$ is the normal vector of boundary Γ_1 or Γ_2. The temperature at the inlet boundary is set constant $T = T_0$. The remaining part of the boundary $\partial\Omega \setminus (\Gamma_1 \cup \Gamma_2)$ is a no-flow ($\mathbf{u} \cdot \mathbf{n} = \mathbf{0}$) and isolating ($\frac{\partial T}{\partial \mathbf{n}} = 0$) boundary. The heat source in Ω_h represents the area that generates the heat and gives rise to the cooling problem. This domain may be included for design or kept as a passive solid zone depending on the problem approached.

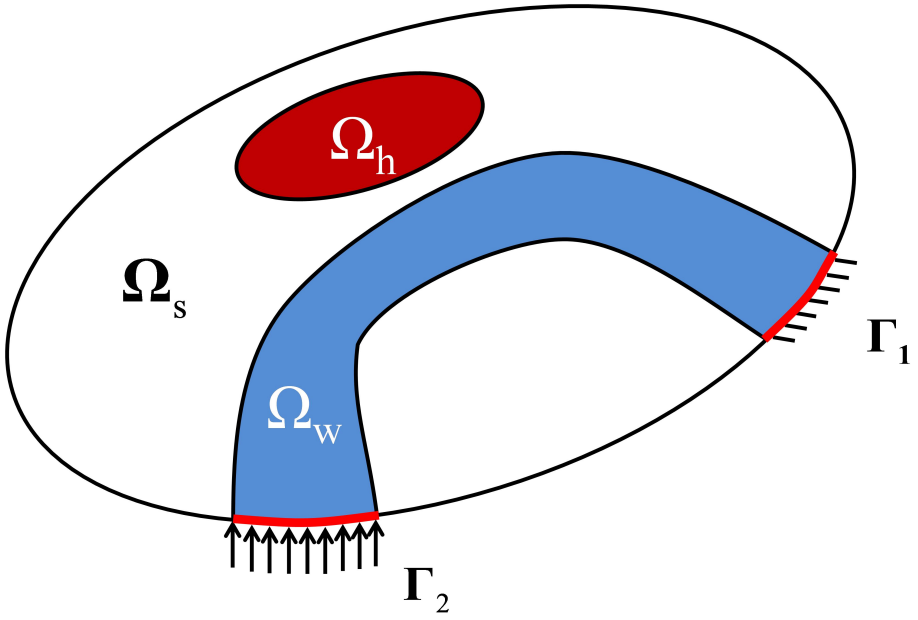

Figure 1: Generic cooling system design. Ω_w and Ω_s denote the fluid and solid domains, respectively, while Ω_h denotes a heat source (solid). Γ_1 and Γ_2 denote outflow and inflow boundaries, respectively.

2.1. Heat transfer model with Darcy flow

An internal flow problem is generally modeled using the incompressible steady-state Navier-Stokes equations:

$$\rho \mathbf{u} \cdot \nabla \mathbf{u} = -\nabla p + \mu \nabla^2 \mathbf{u} - \rho \mathbf{b}, \tag{1}$$

$$\nabla \cdot \mathbf{u} = 0, \tag{2}$$

where $\mathbf{u}$ denotes the velocity field and p the pressure, μ is the dynamic viscosity, ρ is the mass density and the vector $\mathbf{b}$ is the body force per unit mass. Viscosity of the cooling fluids depends on temperature in general. The equations may be solved assuming iso-thermal conditions as the temperature dependence is rather weak for small temperature variations.

For active cooling strategies based on pumping of the fluid through the channels, a turbulent flow model is generally needed to model the internal fluid mixing as well as the thin boundary layer where most heat is exchanged. The velocity is determined by friction in turn resulting in a pressure loss (gradient) across the component. In practice, turbulence models such as Reynolds-averaged Navier-Stokes (RANS) can be utilized to simulate this flow. However, solving the non-linear Navier-Stokes equations is difficult in a topology optimization setting and very time-consuming. For early conceptual design of cooling layouts, fast simulation and low turnaround time are critical and hence a computationally efficient model with acceptable accuracy is required.

Considering that the velocity profile of a fully turbulent flow is much flatter than the parabolic fully developed laminar profile, we propose to approximate the flow as an inviscid one by a Darcy potential flow model:

$$\mathbf{u} = -\frac{\kappa}{\mu}\nabla p, \tag{3}$$

where the velocity is proportional to the pressure gradient by the ratio of the permeability κ and the viscosity μ. Inserting this into the incompressibility condition and by ignoring the body force term yields the following model:

$$\nabla \cdot \left(-\frac{\kappa}{\mu}\nabla p\right) = 0. \tag{4}$$

The velocity profile of a Darcy flow in a confined channel is uniform and flat without any boundary effects at all. However, by careful selection of the artificial permeability of fluid and solid regions, it is possible to mimic the turbulent flow conditions sufficiently well. Tuning and comparison between the Darcy flow model and a turbulent RANS model is included in section 2.3.

Based on above Darcy flow model, the corresponding temperature field is described by a convection-diffusion model as:

$$\rho c_p \mathbf{u} \cdot \nabla T = k\nabla^2 T + Q, \tag{5}$$

where T is the temperature field, k the thermal conductivity, c_p is the specified heat and Q is the volumetric heat source intensity. Together with (3), the convective heat-transfer model becomes:

$$\rho c_p \left(-\frac{\kappa}{\mu}\nabla p\right) \cdot \nabla T = k\nabla^2 T + Q. \tag{6}$$

2.2. Finite element analysis

With the standard Galerkin method, the finite element model is derived as:

$$\mathbf{K_p p} = \mathbf{f_p}, \tag{7}$$

$$(\mathbf{K_t} + \mathbf{C}(\mathbf{p}))\,\mathbf{t} = \mathbf{f_t}, \tag{8}$$

where $\mathbf{K_p}$ is the permeability matrix and $\mathbf{K_t}$ the conductivity matrix. $\mathbf{p}$ is the pressure vector and $\mathbf{t}$ is the temperature vector. $\mathbf{f_p}$ and $\mathbf{f_t}$ are the load vectors for the pressure and temperature fields, respectively. $\mathbf{C}(\mathbf{p})$ is the matrix of the convection term which depends on the pressure field. The equation system is solved sequentially by first obtaining the pressure $\mathbf{p}$ and then the temperature field $\mathbf{t}$.

The matrices are obtained by assembling the element matrices

$$\mathbf{K_p} = \sum_{n=1}^{N_e} \mathbf{k}_\mathbf{p}^e = \sum_{n=1}^{N_e} \int_{\Omega^e} \frac{\kappa}{\mu} \mathbf{B}^{\mathrm{T}} \mathbf{B} \mathrm{d}\Omega, \tag{9}$$

$$\mathbf{K_t} = \sum_{n=1}^{N_e} \mathbf{k}_\mathbf{t}^e = \sum_{n=1}^{N_e} \int_{\Omega^e} k \mathbf{B}^{\mathrm{T}} \mathbf{B} \mathrm{d}\Omega, \tag{10}$$

$$\mathbf{C}(\mathbf{p}) = \sum_{n=1}^{N_e} \mathbf{c}^e(\mathbf{p}^e) = \sum_{n=1}^{N_e} \int_{\Omega^e} \hat{\mathbf{N}}^{\mathrm{T}} \rho c_p \left(-\frac{\kappa}{\mu} \mathbf{B} \mathbf{p}^e \right)^{\mathrm{T}} \mathbf{B} \mathrm{d}\Omega, \tag{11}$$

where N_e is the number of elements, $\mathbf{N}$ is the shape function matrix and $\mathbf{B} = \nabla \mathbf{N}$ is the gradient of the shape function matrix. The superscript e denotes element matrices or vectors.

As the convection-diffusion problem is convection dominated, a streamline upwind stabilization term [8, 19] is applied to alter the shape function in (11) as:

$$\hat{\mathbf{N}} = \mathbf{N} + \frac{\mathrm{h_e}}{2} \left(\frac{\mathbf{u}}{\|\mathbf{u}\|} \right)^{\mathrm{T}} \mathbf{B}, \tag{12}$$

where $\mathrm{h_e}$ is the size of the element, $\mathbf{u}$ is elemental average velocity vector along each coordinate direction and $\|\mathbf{u}\| = \sqrt{\mathbf{u}^{\mathrm{T}}\mathbf{u}}$ is the magnitude of velocity. The right hand term of (7) is based on the inlet velocity:

$$\mathbf{f_p} = \int_{\Gamma_2} \mathbf{N}^{\mathrm{T}} \left(\mathbf{n} \cdot \mathbf{u}_{in} \right) \mathrm{d}\Gamma, \tag{13}$$

and the thermal loading, i.e. the right hand term of (8), is given as:

$$\mathbf{f_t} = \int_{\Omega_\mathrm{h}} \mathbf{N}^{\mathrm{T}} Q \mathrm{d}\Omega. \tag{14}$$

2.3. Model equivalence and material property studies

To verify the performance and accuracy of the Darcy flow model, it is compared to a full-blown turbulent flow benchmark example with the same boundary conditions. The setup is shown in Fig. 2(a), where a square domain provides a heat source Ω_h at the center. The fluid Ω_w flows from the left inlet to the outlet at the right end of a U-shaped channel. The radius of channels and fillets

Table 1: Material properties for steel and water. Below the line the model specific properties for permeability and viscosity are listed.

	Unit	Turbulent flow	Darcy Flow
k_w	$\mathrm{W/m{\cdot}K^{-1}}$	0.6	0.6
k_s	$\mathrm{W/m{\cdot}K^{-1}}$	44	44
c_{pw}	$\mathrm{J/kg{\cdot}K^{-1}}$	4200	4200
c_{ps}	$\mathrm{J/kg{\cdot}K^{-1}}$	460	460
ρ_w	$\mathrm{kg/m^3}$	1000	1000
ρ_s	$\mathrm{kg/m^3}$	7800	7800
μ_w	Pa·s	0.001	0.001
μ_s	Pa·s	-	0.001
κ_w	$\mathrm{m^2}$	-	2.5×10^{-5}
κ_s	$\mathrm{m^2}$	-	2.5×10^{-11}

are set as $R_1 = 0.2D$, $R_2 = 0.1D$, $R_3 = 0.025D$, where $D = H = 0.5\mathrm{m}$ is the width of the design domain. The prescribed velocity at the inlet, of width L_{in}, is $\mathbf{u}_{in} = (0, u_0)^T$, with $u_0 = 0.2\mathrm{m/s}$ and the temperature is $T_{in} = 0$, corresponding to a Reynolds number of $Re = \frac{\rho L_{in} u_0}{\mu} = 20,000$. The outlet is modeled by prescribing the pressure to $p_{out} = 0$. The heat source generates a heat flux of $Q = 200\mathrm{kW/m^3}$ and it shares material properties with the solid phase. The material properties used are chosen to be similar to steel and water as listed in Tab. 1.

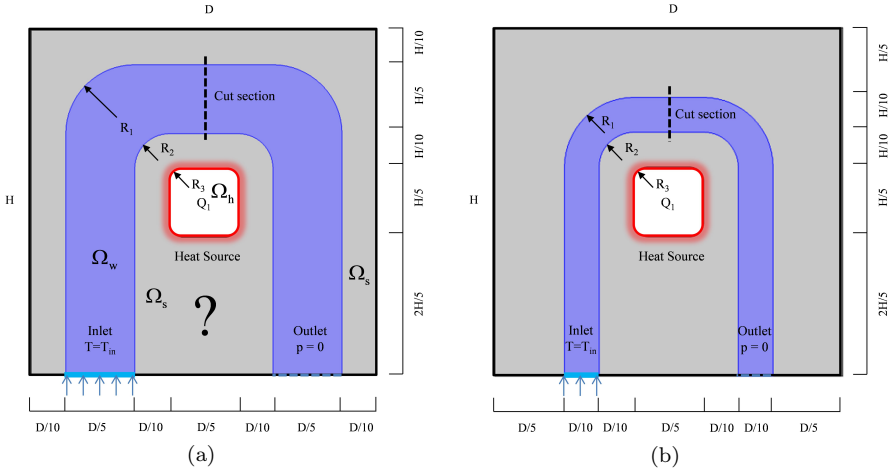

Figure 2: Problem settings used for comparison of models and tuning of parameters. Inlet with prescribed flow velocity $\mathbf{u}_{in}$ and temperature T_{in}. Outlet is an pressure outlet boundary with $p = 0$. Design (a) has a large inlet and channel width. Design (b) has a thin channel.

To make a good equivalent model, the pressure, velocity and temperature

fields should all ideally be close to those of the RANS model. We propose the following procedure for obtaining the material properties needed for the Darcy model. Three physical quantities of the Darcy and RANS models are chosen as indicators of their similarity. They are the average velocity at the cross-section indicated by a dashed line in Fig. 2, the pressure drop from the inlet to the outlet, and the temperature at the center of the heat source, respectively.

First, since a convective heat transfer model requires an accurate flow velocity field, the permeability ratio is tuned in a way that ensures good agreement between the flow velocities. As shown in Fig. 3, as $\frac{\kappa_w}{\kappa_s}$ grows, the error between the two models is reduced both on a body-fitted mesh and a structured regular (bi-linear) mesh in the Darcy model (see meshes in Fig. 4). When $\frac{\kappa_w}{\kappa_s} \geq 10^5$, the indicators become similar and thus we fix the permeability ratio to 10^6.

Second, the permeabilities of the water and solid phases in the Darcy flow model are adjusted to make the pressure drops similar, which corresponds to finding κ_w and κ_s such that:

$$\Delta p_{\mathrm{T}} \approx \Delta p_{\mathrm{D}}, \tag{15}$$

where Δp is the pressure drop between the inlet and outlet expressed as:

$$\Delta p = \frac{1}{|\Gamma_2|} \int_{\Gamma_2} p \mathrm{d}\Gamma - \frac{1}{|\Gamma_1|} \int_{\Gamma_1} p \mathrm{d}\Gamma. \tag{16}$$

The pressure fields of the two models are compared in Fig. 4 column (a) and (b). The pressure fields do not match perfectly because the Darcy flow model cannot reflect the boundary and inertia effects of the turbulent flow model. However, the pressure drop can be mimicked by appropriate choice of the artificial permeability in the water phase. The pressure drop is found to be linearly related to κ_w or κ_s when the permeability ratio is constant. By artificially adjusting κ_w, until $\Delta p_{\mathrm{T}} = \Delta p_{\mathrm{D}}$, the permeability of the water phase is finally chosen as $\kappa_w = 2.5 \cdot 10^{-5}\mathrm{m}^2$ and hence for the solid phase $\kappa_s = 2.5 \cdot 10^{-11}\mathrm{m}^2$.

The detailed simulation results i.e. mesh, pressure field, velocity field, temperature field and heat flux of both the turbulent and the Darcy flow models are shown in Fig. 4. The simulation results of the RANS and Darcy models by using a body-fitted mesh are compared in Fig. 4(a) and (b). The simulation using the Darcy model on a structured mesh is given in Fig. 4(c).

As shown in Fig. 4(a) and (b), the temperature and velocity fields of the two models exhibit visual agreement except for the low speed flow region along the left boundary of the outlet pipe. However, the pressure fields do not fully match except for the pressure drop between the inlet and outlet. The trajectories of the convective heat flux shown in the fifth row of Fig. 4 share the same trend in mainly concentrating at the interface between the liquid and solid phase near the heat source. However, the magnitude of heat flux between Fig. 4(a) and (b) varies due to the inability of describing the inertial effect by the Darcy model. As observed in the velocity field, there is a clear low velocity zone near the left wall of the right channel, which causes a high local temperature and thus

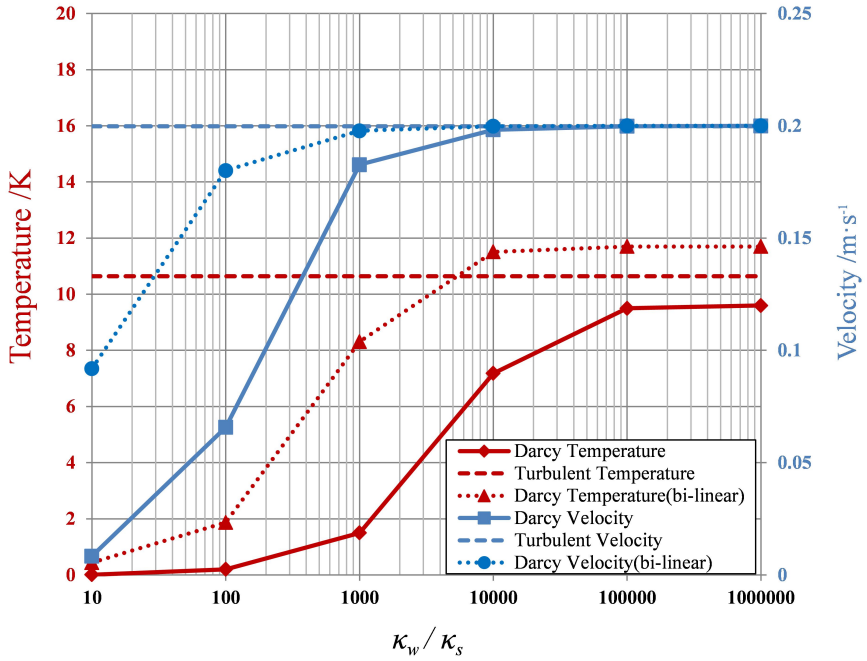

Figure 3: Comparison of two indicators obtained for the turbulent flow model and the simplified Darcy model as a function of permeability ratio. $\kappa_w = 2.5 \cdot 10^{-5}\mathrm{m}^2$

a different heat flux distribution. In column (c), noise is observed from using a structured regular mesh with a jagged boundary, which causes oscillations in the temperature and velocity fields. The oscillation values are relatively small in the liquid phase compared to the solid phase. It is worth noting that using a structured mesh may cause oscillations in the temperature field in the liquid phase and this error may be amplified into the heat flux field. Nevertheless, these errors do not seem to jeopardize the proposed cooling channel optimization in a significant way because the temperature field generally seems well described by the equivalent model and this is a dominating factor in the optimization process.

Apart from the turbulent flow effect, local recirculation may also affect the heat exchange. Recirculation in channel flow usually occurs wherever there are sudden changes of channel width, sharp corners or obstacles. In order to avoid recirculation, length scale control is adopted in this paper in order to yield designs with nearly uniform channel sizes. The details of the length scale control will be introduced in section 3.4.

To show the effectiveness of the equivalent model under different flow conditions, the effect of Reynolds number Re and the channel sizes are further studied with the channels shown in Fig. 2. Three levels of Reynolds number

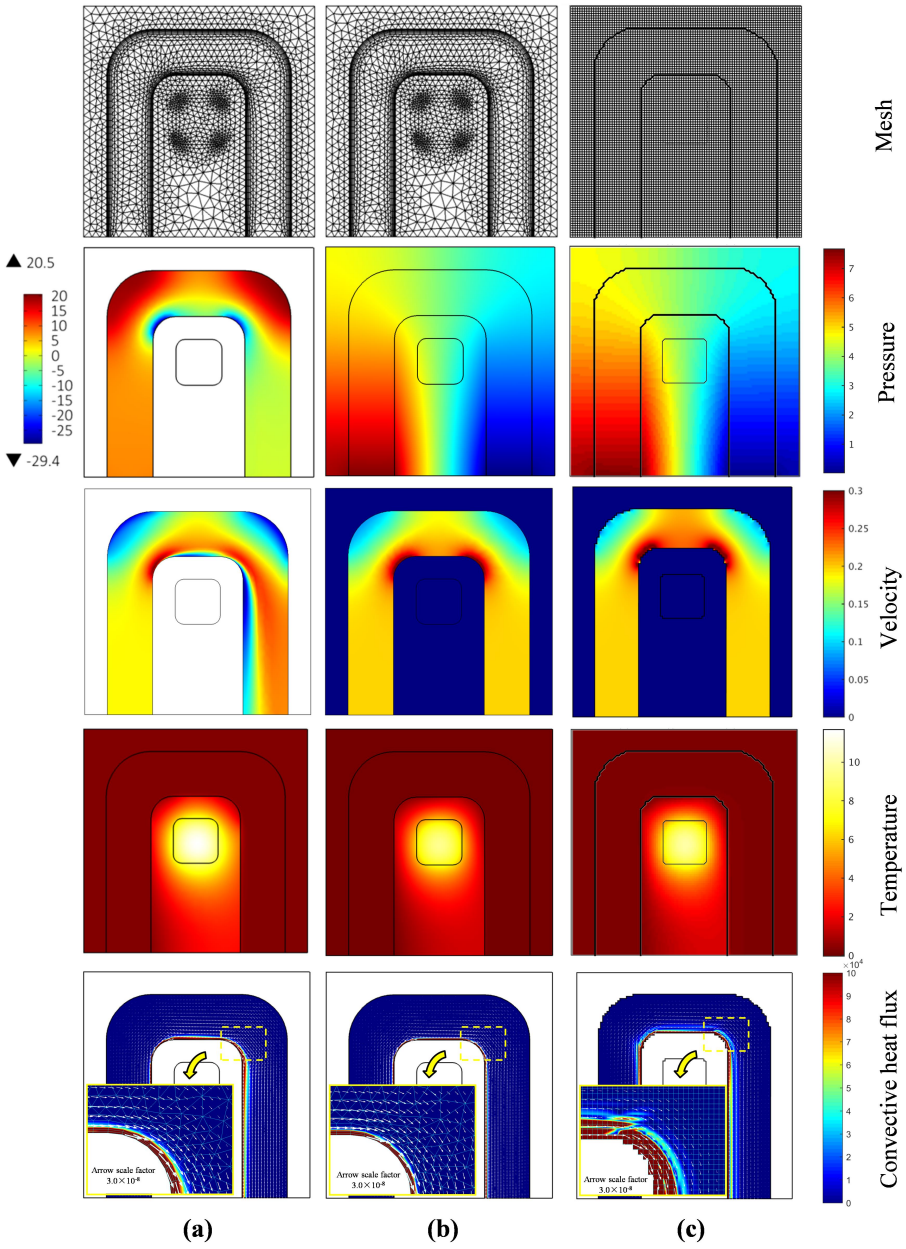

Figure 4: Comparison of models: (a) Turbulent flow model (RANS) with CFD mesh, (b) Darcy flow model with body-fitted mesh, (c) Darcy flow with structured regular mesh. For the second row, the color legend on the left is for the RANS model and the one on the right is for the Darcy models.

Table 2: Error analysis of flow conditions.

Analysis cases	u_0 [m/s]	Re	E_T
Wide channel	0.20	20,000	7.5%
	0.50	50,000	4.0%
	1.00	100,000	2.3%
Narrow channel	0.40	20,000	2.8%
	1.00	50,000	1.2%
	2.00	100,000	0.7%

$Re = 20,000$, $Re = 50,000$ and $Re = 100,000$ are compared by changing the velocity boundary condition. Two channel sizes are shown in Fig. 2, in which the geometry of Fig. 2(b) has half of the channel width of that in Fig. 2(a). The results are given in Tab. 2, where a temperature field indicator is used to compare the accuracy of the equivalent model. The indicator is defined as the relative error of the equivalent model: $E_T = \frac{|T_R - T_D|}{T_R} \times 100\%$, where T_R and T_D are the temperatures at the center of the heat source of the RANS and Darcy model, respectively. Note that, a body fitted mesh and a structural regular mesh are used here for the RANS and the equivalent models, respectively. The result shows that the error of the temperature field decreases when the Reynolds number increases. Furthermore, for constant Re, the case with a narrower channel has a lower error in temperature, which is intuitively understandable since this case will have more uniform flow and less back-circulation. Despite the inaccuracies, the proposed model is nevertheless acceptable in an optimization process, as will be discussed and demonstrated in section 4.3.

3. Topology Optimization

3.1. Parametrization and Material interpolation

The generic cooling system domain Ω shown in Fig. 1 is governed monolithically by the Darcy flow based convection model. In order to perform topology optimization, each finite element is annotated with a continuous physical density $\hat{\xi}_e \in [0, 1]$ indicating whether it is filled with water $\hat{\xi}_e = 0$ or solid $\hat{\xi}_e = 1$. A projection approach [13, 23] is employed to relate the element-based design variables $\xi \in [0, 1]$ to the physical densities $\tilde{\xi}_e$ by a smoothed Heaviside function:

$$\tilde{\xi}_e = \frac{\tanh(\beta\eta) + \tanh\left(\beta\left(\hat{\xi}_e - \eta\right)\right)}{\tanh(\beta\eta) + \tanh(\beta(1-\eta))}, \tag{17}$$

where

$$\hat{\xi}_e = \frac{1}{\sum\limits_{i \in N_e} H_{ei}} \sum_{i \in N_e} H_{ei}\xi_i, \tag{18}$$

In the above equations, the weighting function H is determined by the distance between the element e and its neighbourhood elements:

$$H_{ei} = \begin{cases} r_{\min} - \|\mathbf{x}_i - \mathbf{x}_e\|, & \|\mathbf{x}_i - \mathbf{x}_e\| \leq r_{\min} \\ 0 & \text{otherwise} \end{cases} \tag{19}$$

where $r_{\min}$ is the filter radius. In addition, the parameter β in (17) denotes the steepness of the smoothed Heaviside function and η is the threshold value.

The physical density value $\tilde{\xi}_e$ is used to determine the material properties of the governing equations. The permeability, conductivity, density and specific heat capacity are defined by individual interpolation functions as:

$$\kappa = \kappa_s + \left(1 - \tilde{\xi}\right)^{p_\kappa} (\kappa_w - \kappa_s) \tag{20}$$

$$k = k_w + \tilde{\xi}^{p_k} (k_s - k_w) \tag{21}$$

$$\rho = \rho_w + \tilde{\xi}^{p_\rho} (\rho_s - \rho_w) \tag{22}$$

$$c_p = c_{pw} + \tilde{\xi}^{p_{c_p}} (c_{ps} - c_{pw}) \tag{23}$$

where p_κ, p_k, p_ρ and p_{c_p} are penalization parameters. In this paper, linear interpolations $p_k = p_\rho = p_{c_p} = 1$ are used for conduction, density and specific heat. A larger value $p_\kappa = 3$ is used for stronger penalization of permeability. Based on the author's experiences, it is difficult to get clear topologies with lower p_κ values.

3.2. Optimization objective

In this paper, we focus on minimizing the mean temperature in the domain Ω^* using the objective functional[5]:

$$\phi = \frac{1}{|\Omega^*|} \int_{\Omega^*} T \mathrm{d}\Omega \approx \frac{1}{N_1} \mathbf{L}_1^{\mathrm{T}} \mathbf{t} \tag{24}$$

where $\mathbf{L}_1$ is an index vector with 1's in nodes corresponding to the area considered, e.g. the heat source and N_1 being the number of these nodes.

The optimization problem is now stated as:

$$\begin{array}{lll} \min\limits_{\boldsymbol{\xi} \in \mathbb{R}^{N_e}} & : & \phi \\ \text{s.t.} & : & \mathbf{K_p p} = \mathbf{f_p} \\ & & (\mathbf{K_t} + \mathbf{C(p)})\, \mathbf{t} = \mathbf{f_t} \\ & & \dfrac{\sum\limits_{e=1}^{\mathrm{N_e}} \left(1 - \tilde{\xi}_e\right)}{(1-f)\, N_e} - 1 \leq 0 \\ & & h_j \leq 0, \qquad\qquad j = 1, 2, ..., M \\ & & 0 \leq \xi_e \leq 1, \qquad\qquad e = 1, 2, ..., N_e \end{array} \tag{25}$$

[5]The optimization objective for the cooling channel design could be any function of volume, pressure or temperature.

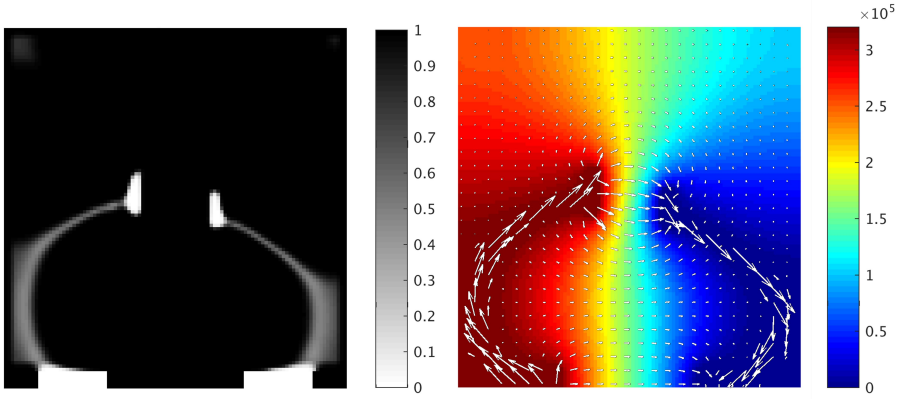

Figure 5: Disconnected of water phase $\tilde{\xi}$ distribution and pressure field(Pa)

where f is a predefined minimum volume fraction of solid and h_j represents M generic inequality constraints to be discussed later.

The adjoint method[20] is used to calculate the sensitivities of objective functional and constraints where the details can be seen in Appendix A. The optimization problem is solved using the Method of Moving Asymptotes (MMA)[24].

3.3. Pressure drop constraint

The pressure drop is an indicator of the energy cost for pumping fluid through the cooling system. A functional evaluating the pressure drop constraint, assuming that the outflow condition is $p = 0$, can be written as:

$$h_1 = \frac{1}{|\Gamma_2|}\int_{\Gamma_2} p \, \mathrm{d}\Gamma - h^* \approx \frac{1}{N_2}\mathbf{L}_2^{\mathrm{T}}\mathbf{p} - h^* \tag{26}$$

Where $\mathbf{L}_2$ is a vector representing the velocity inlet nodal set index, N_2 is the number of nodes and h^* is the target pressure drop value.

The pressure drop constraint has a great impact on the channel shape in the Darcy flow model. If a large pressure drop is allowed, the water phase may not form a continuous domain e.g. a channel, but rather disconnect the phase, as shown in Fig. 5. This phenomenon occurs because the porous flow model still allows flow through the solid phase elements at the cost of a large pressure drop. However, this can be alleviated by imposing a suitable pressure drop constraint on the optimization problem.

3.4. Length scale control

With the proposed Darcy-flow based heat transfer model, narrow channels surrounding the heat sources are sufficient for transferring the heat that diffuses into the fluid. Such narrow channels however, are difficult to manufacture in practice. Furthermore, as will be seen in later sections, applying the pressure

constraint alone is unable to eliminate gray elements or to ensure channels of a certain width. Therefore, it is critical to impose a strict minimum length scale, in turn ensuring easily manufacturable designs.

The geometric constraint proposed by [30] is employed here to strongly impose minimum length scale for the cooling channels:

$$h_2 = \frac{1}{N_e}\sum_{e=1}^{N_e} I_e \cdot \left[\min\left\{\left(\eta_d - \hat{\xi}_i\right),\ 0\right\}\right]^2 \leq \epsilon, \tag{27}$$

where

$$I = \left(1 - \hat{\xi}\right)\exp\left(-r^4 \cdot |\nabla\hat{\xi}|^2\right). \tag{28}$$

In the above equations, I is a structural indicator function and $r = r_{\min}/h_e$ is the number of elements covered by the filter radius. The threshold value η_d in (17) is a user specified value ($\eta_d < \eta$) discussed below and ϵ is a small number to compensate for numerical errors[6]. The actual minimum length scale on the final design is governed by the filter radius $r_{\min}$, provided that $\eta = 0.5$. According to the discussions in [21], for a desirable length scale b, η_d can be determined based on the following expression:

$$\eta_d = \begin{cases} \frac{1}{4}\left(\frac{b}{r_{\min}}\right)^2 + \frac{1}{2}, & \frac{b}{r_{\min}} \in [0,1] \\ -\frac{1}{4}\left(\frac{b}{r_{\min}}\right)^2 + \frac{b}{r_{\min}}, & \frac{b}{r_{\min}} \in [1,2] \\ 1, & \frac{b}{r_{\min}} \in [2,+\infty) \end{cases} \tag{29}$$

e.g. a desired length scale of $b = r_{\min}$ is obtained for $\eta_d = 0.75$.

4. Numerical examples

4.1. Design of cooling channels for a localized heat source

The proposed method is first applied to design of fluid channels for cooling a square heat source. The problem is the same as shown in Fig. 2(a), whilst the set-up for topology optimization is illustrated in Fig. 6. The heat source is located at the center of the design domain. The boundary conditions are applied on the outer edges of two extended non-design domains (blue color), which ensure that the flow essentially comes from one source even if it may split when entering the design domain.

The U-shape model shown in Fig. 2(a) has a pressure drop of 8.17Pa and the volume fraction of its water phase is 0.425. Inspired by this reference we impose a pressure drop constraint of $h^* = 8.00$Pa and upper bound the fluid volume fraction to 0.2, i.e. $f = 0.8$. The design domain is discretized using

[6]Theoretically for a continuous formulation, a minimum length scale is strictly satisfied if $\epsilon = 0.0$. However, in practice due to discretization error, it is pertinent to relax the constraint by a small number ϵ. More details can be found in [30].

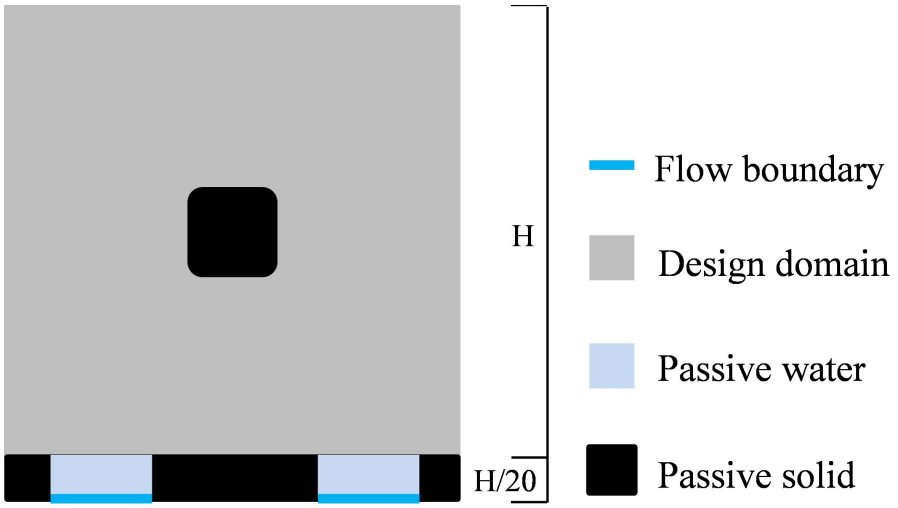

Figure 6: Design domain and passive domains

100×100 4-node rectangular elements. The filter radius is set to $r_{\min} = 0.02$m, corresponding to a minimum length scale of 4-element lengths. The projection parameter β is set to 16 from the beginning of the optimization and the MMA parameters are modified as suggested in [14]. An external move limit of 0.05 is implemented for these examples. The geometric constraint parameter $\epsilon = 10^{-6}$ is chosen according to the suggestions in [30].

In the following two sub-sections, the optimization results with different initial guesses as well as several continuation strategies are compared to investigate the behavior of the proposed approach and find appropriate parameter settings.

4.1.1. Uniform initial guess

The optimization results for a uniform (gray) starting guess, using different strategies and constraint values are shown in Fig. 7, while the specifics of the individual strategies are listed in Tab. 3. The first column in Fig. 7(A1-D1) represents the initial guesses for each case while the second column shows the converged designs without imposing the geometric constraint. The stopping criterion is based on the change in objective functional going below $\Delta\phi \leq 0.001$ and all constraints being satisfied. The third and the fourth columns represent the optimized designs when the pressure constraint (by continuation) and the geometric constraint have been imposed, respectively. The corresponding optimization statistics including values of objective and constraint functions are listed in Tab. 4.

For case A, the optimization starts with the target pressure constraint $h^* = 8.00$Pa and no continuation strategy is used. The optimized design shown in Fig. 7(A2) exhibits a clear topology but gray elements and loosely connected thin channels appear around the heat source. These are non-physical and un-

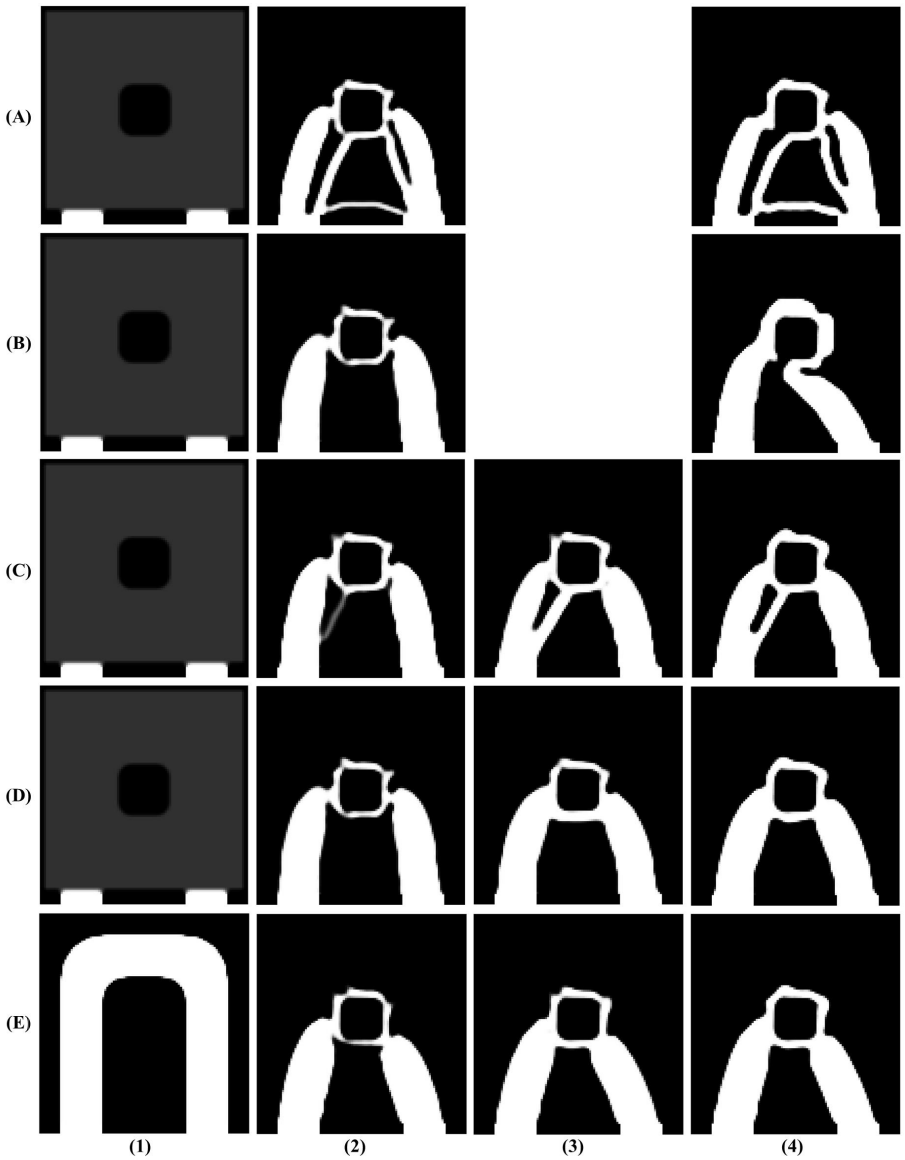

Figure 7: The optimized topology after step (1)∼(4) of strategy A∼E.

Table 3: Optimization strategies

Strategy	A	B	C	D	E
Initial/step 1	uniform	uniform	uniform	uniform	U-shape
	$\beta = 16$	$\beta = 16$	$\beta = 16$	$\beta = 16$	$\beta = 1$
	$h^* = 8$	$h^* = 16$	$h^* = 12$	$h^* = 16$	$h^* = 16$
Step 2	-	-	-	-	$\beta = 1 \sim 16$
Step 3	-	-	$h^* = 12 \sim 8$	$h^* = 16 \sim 8$	$h^* = 16 \sim 8$
Step 4	IGC	IGC	IGC	IGC	IGC

IGC: Implement geometric constraint

Table 4: Performance for optimized resigns using Strategy A∼E including volume, pressure drop and geometric constraint value.

	Obj.	Vol.	Δp	h_2
(A-1)	2.92	0.18	187.50	-
(A-2)	1.88	0.20	8.00	-
(A-4)	1.92	0.20	6.50	1×10^{-6}
(B-1)	2.92	0.18	187.50	-
(B-2)	1.86	0.20	15.99	-
(B-4)	1.90	0.20	16.00	9.98×10^{-7}
(C-1)	2.92	0.18	187.50	-
(C-2)	1.86	0.20	12.00	-
(C-3)	1.88	0.20	8.00	-
(C-4)	1.88	0.20	8.00	9.99×10^{-7}
(D-1)	2.92	0.18	187.50	-
(D-2)	1.86	0.20	15.99	-
(D-3)	1.89	0.20	8.00	-
(D-4)	1.89	0.20	8.00	9.99×10^{-7}
(E-1)	4.70	0.425	8.17	-
(E-2)	1.85	0.20	16.00	-
(E-3)	1.88	0.20	8.00	-
(E-4)	1.88	0.20	8.00	9.98×10^{-7}

desirable from a manufacturing point of view. After introducing the geometric constraint for imposing a minimum length scale, more clear and wider channels are observed, as shown in Fig. 7(A4). It is worth mentioning that a shortcut channel that directly connects the inlet and outlet appears in the converged design. Essentially, this channel contributes little to heat transport since it is far away from the heat source. It appears because of the strong influence of the pressure drop constraint which is satisfied by introducing this bypass. Furthermore, it is found that the geometric constraint has an even stronger impact than the pressure drop constraint on the channel geometry. As seen from Tab. 4, the latter is inactive in the final optimized design because all channels are forced wide enough to ensure a small pressure drop.

Case B shows the optimization with a different pressure drop constraint $h^* = 16.00$Pa. The first design shown in Fig.7(B2) exhibits a clear topology but still with gray elements. In this case, the bypass channel disappears due to the relaxed pressure drop constraint. By introducing the geometric constraint, a topological change is observed as one of the fluid channels gets disconnected. The overall geometry of the channel is also optimized accordingly. It is worth noting that the pressure drop constraint is active for the final design, hence the geometric constraint is not dominating the pressure drop constraint.

Case C starts with a pressure drop constraint $h^* = 12.00$Pa which is tightened to $h^* = 8.00$Pa after the initial convergence (i.e. reaching the stopping criterion). Fig. 7(C2) shows the first converged design that contains a thin gray channel. After the pressure drop constraint is tightened, the channel becomes wider in order to satisfy the constraint. Gray elements still exist in Fig. 7(C3) but disappear after introducing the geometric constraint, as shown in Fig. 7(C4). A clear topology with a strict minimum length scale is obtained at the end.

Case D starts with a pressure drop constraint of $h^* = 16.00$Pa and the first result is the same as that of Case B, shown in Fig. 7(D2). Then, the pressure drop constraint is tightened to $h^* = 8.00$Pa as in Case C. The optimized design in Fig. 7(D3) exhibits a channel surrounding the heat source without resorting to additional channels. After the geometric constraint is applied, the channels surrounding the heat source eventually satisfy the same length scale, which is shown in Fig. 7(D4).

4.1.2. U-shape initial guess

In this subsection, a U-shaped channel initial design as shown in Fig. 7(E1) is used as starting guess and the corresponding results are listed in the fifth row of Fig. 7. An upper pressure drop value $h^* = 16.00$Pa is initially set and β continuation increasing from 1 to 16. The converged design shown in Fig. 7(E2) exhibits a similar topology as in the initial guess study Case D2. Then, the pressure drop constraint is adjusted to $h^* = 8.00$Pa, for which the optimized design shown in Fig. 7(E3) is only slightly different from (D3). Once the geometric constraint is applied, a clear channel topology is obtained as shown in Fig. 7(E3). The length scale of the design is also well controlled. The

final optimized design is similar to that of Case D and both designs perform almost equally with objective values of 1.88 and 1.89, respectively.

4.1.3. Discussion and verifications

From the above study, it can be seen that different optimization strategies lead to different topologies, although with very similar objective values. This indicates a flat optimum with non-unique solutions, which is common in topology optimization where optimized designs may exhibit different topologies but share similar objective values. In the presented cooling channel design, different implementations of the pressure drop constraint lead to different topologies, e.g. Design (A4-C4) and (B4-D4). However, verifications by the RANS model show good cooling performances for all designs. These local minima may be useful in giving engineers more options in an actual design process.

The continuation scheme applied on the pressure-drop constraint affects the final channel distribution significantly. A tight pressure drop constraint will result in extra fluid channels, which may contribute little to the actual heat transfer but mainly to satisfy the target pressure-drop value. First relaxing and then gradually tightening it can result in a more meaningful channel layout. Comparing column (2) or (3) with (4) of Fig.7, gray scale elements are significantly reduced, which indicates that the geometric constraint is important to ensure a clear 0-1 design with a well-controlled minimum length scale.

The pressure, velocity and temperature fields of two initial guesses as well as the optimized design (D4) are given in Fig. 8. The heat source region becomes much cooler after the optimization process which demonstrates the effectiveness of the optimization. Moreover, Fig. 9 compares the verification results of design (D4) using the RANS model and Darcy model. Column (a) and (b) use smooth body-fitted meshes at the interface between solid and water and column (c) uses a structured regular mesh. The pressure drop in the turbulence model is much higher than for the Darcy model due to friction loss and the velocity profiles differs clearly due to the absent inertia exemplified by the flow below the heat source. The velocity boundary effects of the RANS model cannot be fully represented by the Darcy model and as a result, we observe clear differences between the two velocity profiles. Also when a structured regular mesh is used, the velocity profile has oscillation at boundaries due to the jagged edges. Nevertheless, the Darcy model gives the same trend of channel flow including the position of maximum velocity and lower values at corners. Since the heat transfer model is directly related to the velocity field, the temperature fields in the two models are also similar, but with errors due to the mesh resolution. The convective heat fluxes in the two models also exhibit the same trend, except for slight oscillations due to jagged edges of the structured mesh.

4.2. Design of cooling channels with a distributed heat load

4.2.1. Problem description

The proposed approach is further applied to design channels through a square domain ($L = 0.5, H = 0.5$) subject to distributed heating. As shown

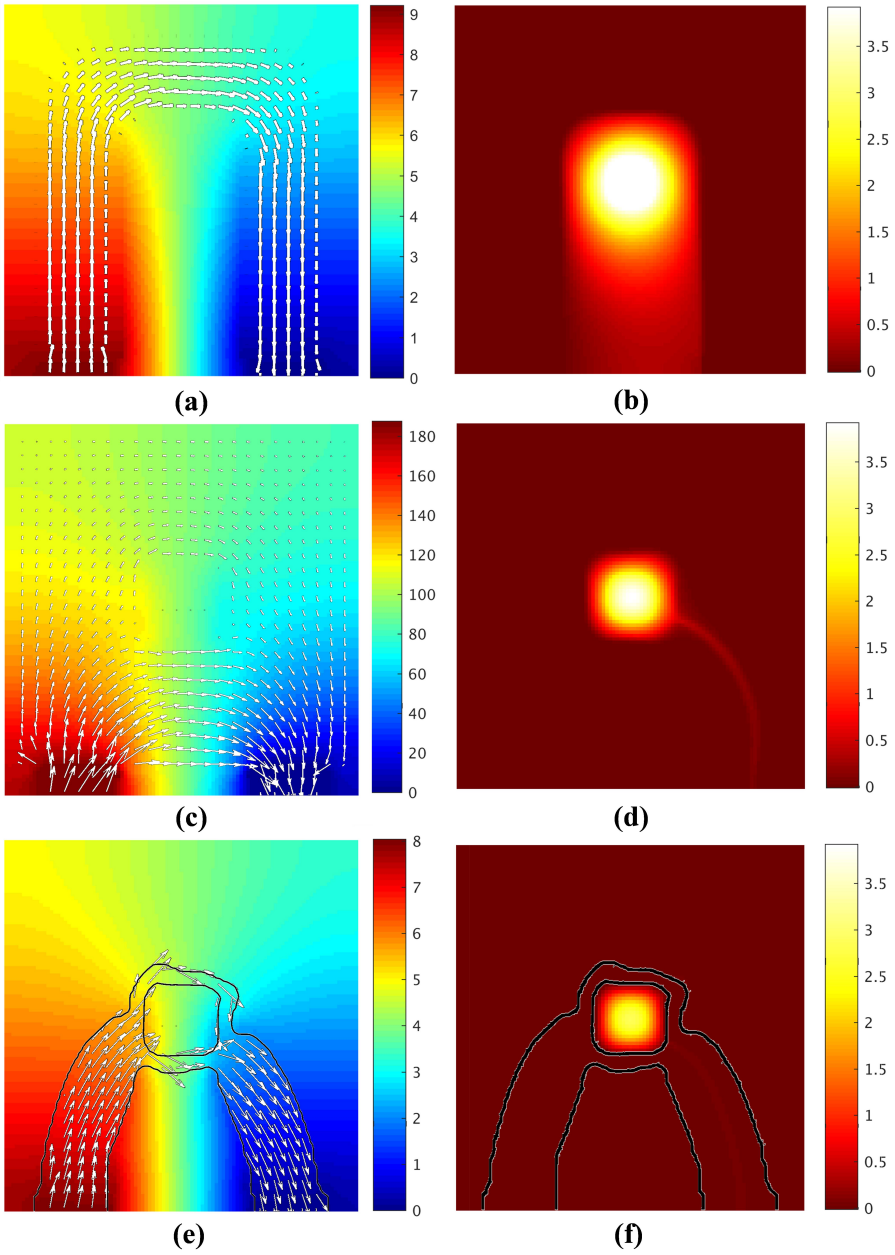

Figure 8: Pressure, velocity (left column) and temperature (right column) distribution:(a-b) U-shape initial guess, (c-d) uniform initial guess, (e-f) optimized result.

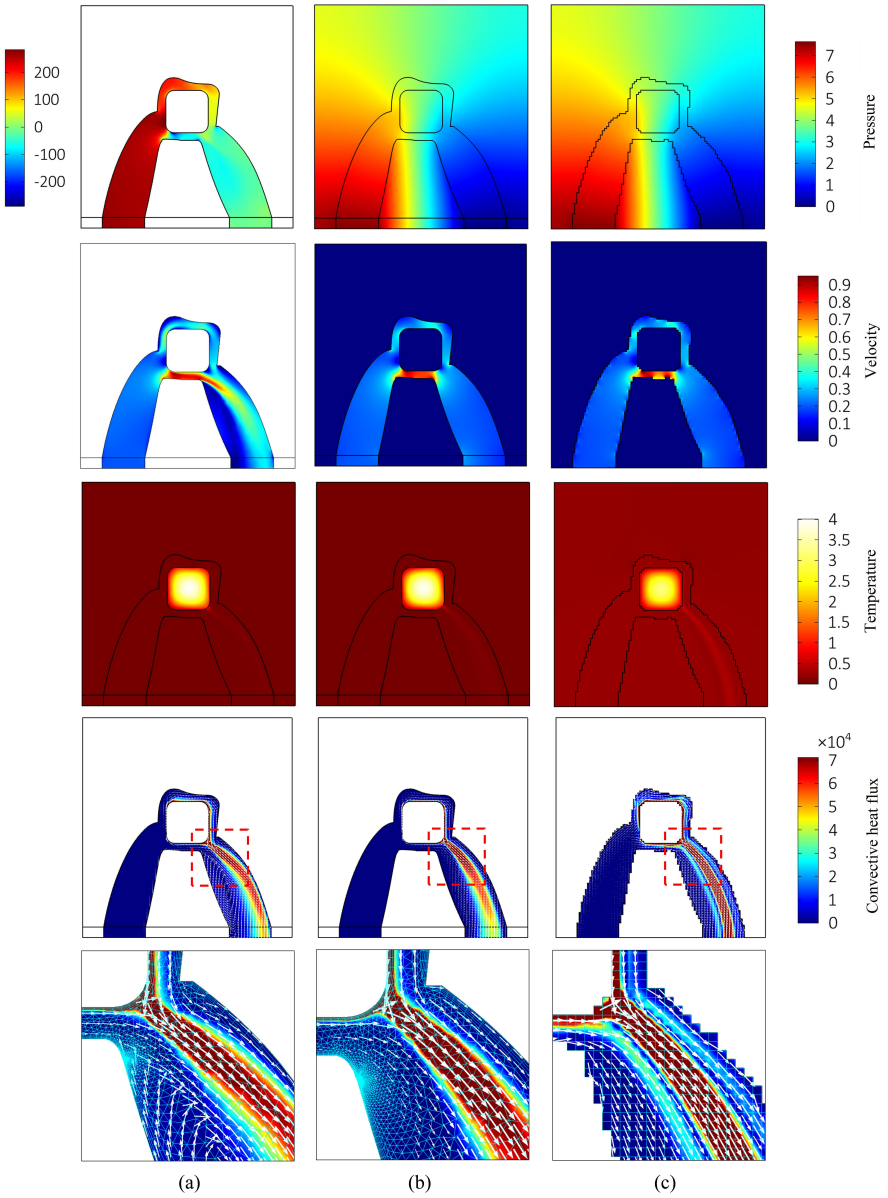

Figure 9: Verification using (a) RANS model with body fitted mesh; (b) Darcy flow model with body fitted mesh; (c) Darcy model with structured mesh. The color legend on the left of the first row is for the pressure field of the RANS model. The legend on the right is for the Darcy model.

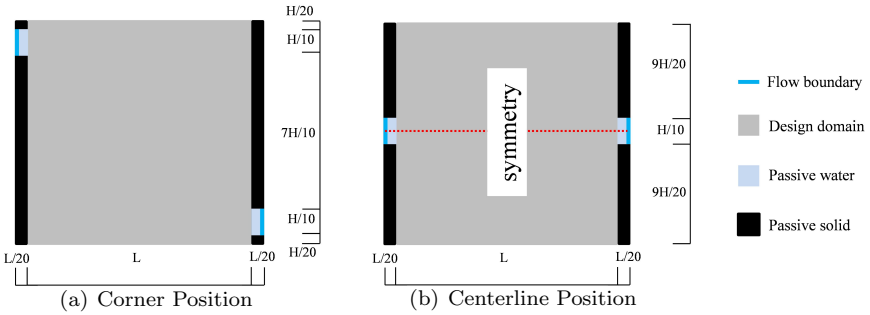

Figure 10: Uniform heat source distribution case with two new inlet and outlet positions: Corner position(a) and centerline position(b)

Table 5: Performance verification of optimized designs in Fig. 11 and Fig. 12

Optimization case	ϕ Darcy	ϕ_{post} RANS	Vol.	Δp Darcy	h_2
Corner position					
Reference design	3.38	7.20	0.56	4.26	-
Uniform $b = 4$	1.81	2.74	0.56	3.55	5×10^{-6}
Uniform $b = 6$	2.10	4.49	0.56	3.39	5×10^{-6}
Initial guess $b = 6$	2.73	3.52	0.56	4.26	5×10^{-6}
Centerline position					
Reference design	4.72	14.72	0.56	2.39	-
Uniform $b = 4$	1.84	3.73	0.56	2.39	5×10^{-6}
Uniform $b = 6$	3.16	6.29	0.56	2.39	5×10^{-6}
Initial guess $b = 6$	2.36	13.34	0.56	2.39	5×10^{-6}

in Fig. 10, two cases with the inlet and outlet located at the *corner* and *centerline* positions are considered, which is an engineering problem given in [25]. The square design domain is heated uniformly by a distributed flux $Q = 20\text{kW/m}^3$ and passive domains are defined for both solid and fluid phases along the vertical boundaries. For comparison, two reference designs, shown in the leftmost columns of Fig. 11 and Fig. 12, are analyzed. Their pressure drops are $h^* = 4.26\text{Pa}$ and $h^* = 2.39\text{Pa}$, respectively. These values are used as reference for the following optimizations. The volume fraction of the water phase is set to 0.44, i.e. $f = 0.56$, which is the same for both reference designs.

4.2.2. Optimization and verification

Fig. 11 and Fig. 12 show the results of the *corner* and *centerline* cases respectively. For each case, three sets of optimized results that come from a uniform gray initial guess as well as the reference design are compared and verified. The designs shown in column (1) and (2) are obtained with the same gray

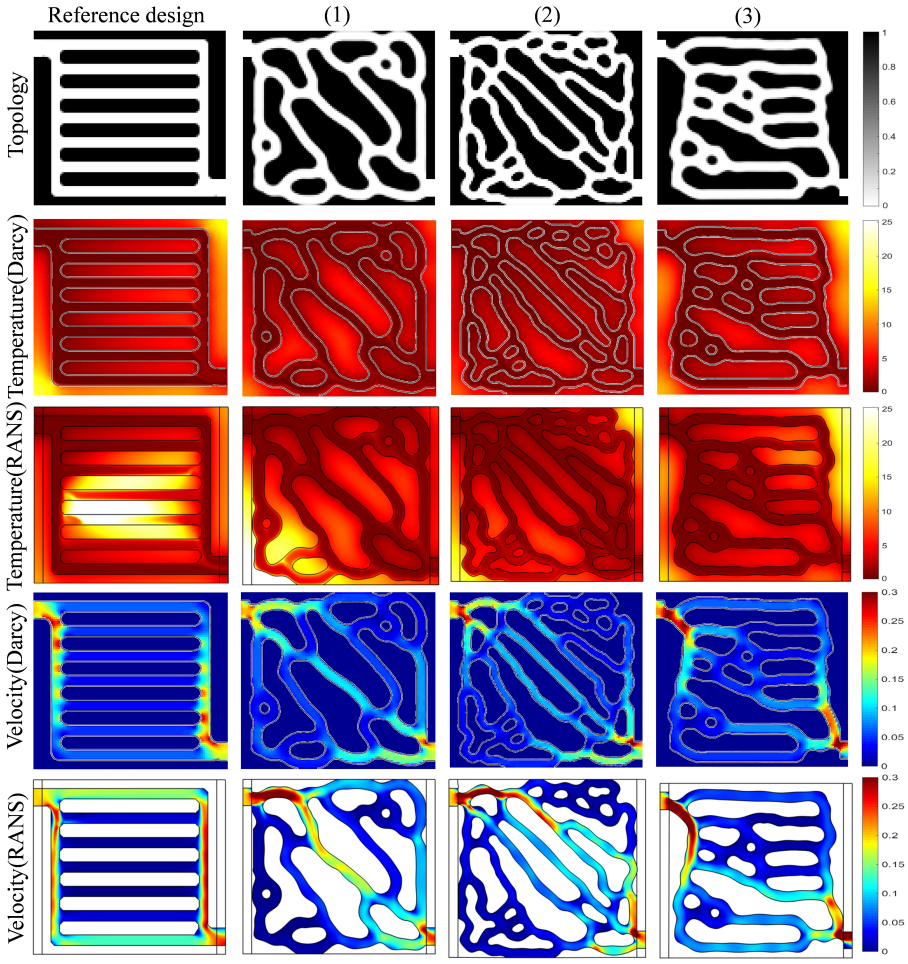

Figure 11: Verification of the Corner-position case using Darcy and RANS models: temperature and flow velocity distributions.

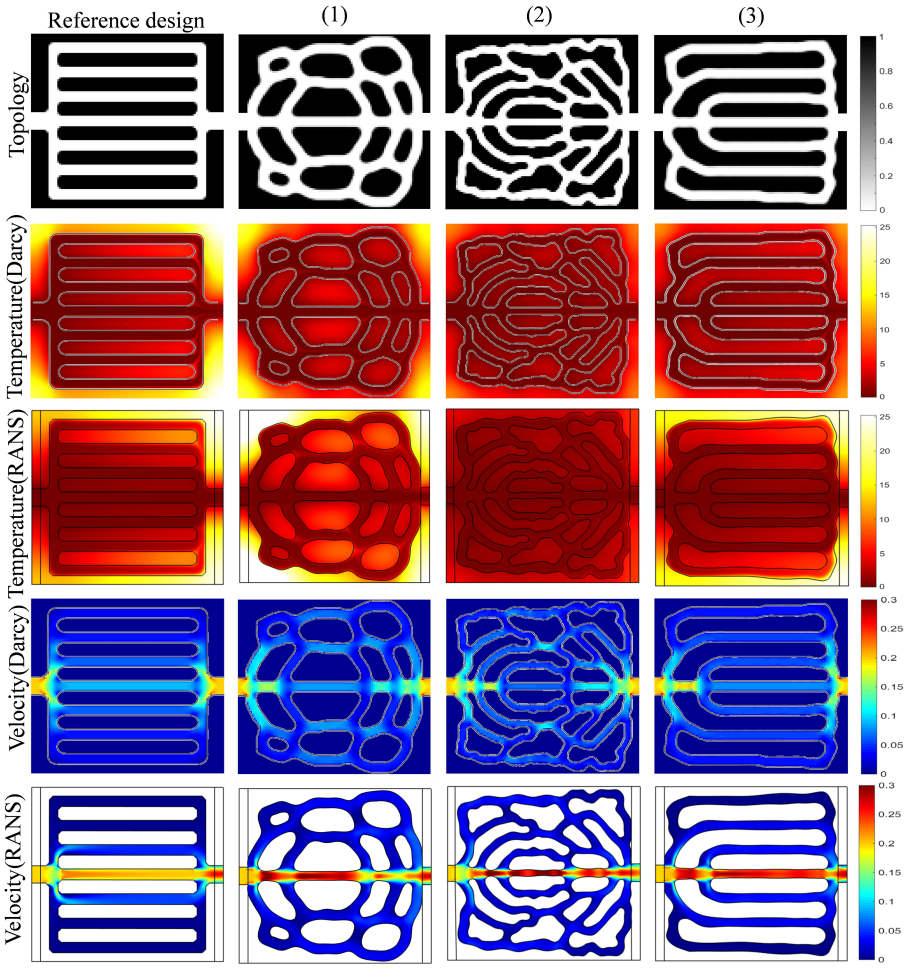

Figure 12: Verification of Centerline-position case using Darcy and RANS models: temperature and flow velocity distributions.

initial guess but different length scales of 4 and 6 elements, respectively. Strategy A from the previous example is applied here (first $\beta = 16$, then geometric constraint). The design in column (3) is initiated with the reference design employing a length scale of 6 elements. The geometric constraint is applied after a proper topology is formed by continuously increasing η_d from 0.5 to 0.75. Note that the reference design has a length scale of 6 elements.

Objective functional and constraints values are summarized in Tab. 5. Both cases exhibit common trends on the various aspects. First, the optimized designs always behave better with lower average temperatures and lower pressure drops than the reference designs under the same or a smaller length scale. This indicates that the proposed method is effective in yielding more efficient heat-transfer channels than simple intuition. Second, by comparing the designs in column (1) and (2), it is apparent that the smaller the channel width, the better the heat transfer capability. This complies with the previous observations on the heat being transported by a thin layer of fluid near the boundary. Also, narrower channels provide better distribution of the cooling agent. Third, the optimized result in column (3) outperforms the intuitive design but performs worse than the two that start from a uniform gray, which underlines that the optimization process is initial-design dependent.

The optimized designs are further verified using the RANS model and the verification results generally follow the same trend as the above observations for the Darcy model. It is noted that the velocity fields shown for the Darcy and RANS models exhibit more differences in Fig.12 than those in the previous U-shape example in (Fig. 9). In the current case, there are more branches in the design domain where the width of each branch has almost the same width as the inlet. The direct flow path from inlet to outlet seems to have much higher velocity than other paths due to inertia. As inertia is absent in the potential Darcy model it is observed that secondary flow paths have higher speeds than those reported by the RANS model, which are almost zero as seen in Fig.12. This difference yields a lower mean temperature for the Darcy model compared to that of using the RANS model. In practice, a full-blown fluid model is required for an accurate heat-transfer simulation. Besides, there are indeed difference between Darcy and RANS flow simulation.

4.3. Discussion

In this section, the impact of the pressure drop constraint is first studied. Fig.13 shows the optimized designs by using three different pressure drop constraints. Design (a) and (c) are obtained with 95% and 105% of the pressure constraint used for design (b), respectively. It is found that the optimized topology varies significantly for different pressure drop constraints. However, all three designs have a similar objective value according to the verification results in Tab. 6 and better cooling capability than the reference design.

To study the effects of Reynolds number, the centerline position case is further studied with three different inlet flow velocities as shown in Fig. 14 (a-c). The pressure drop constraint of each case is chosen according to the pressure drop level of the reference design as shown in Fig. 11. Besides, the optimization

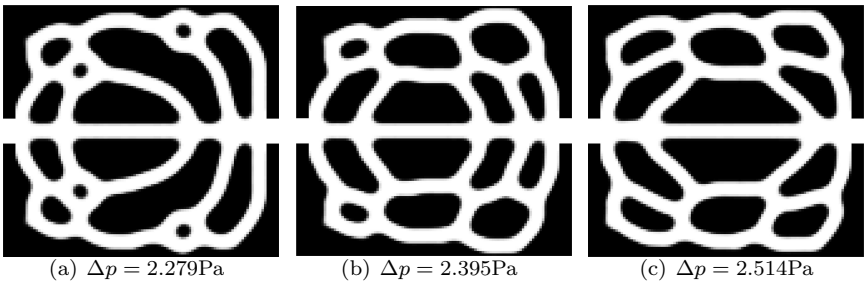

(a) $\Delta p = 2.279$Pa (b) $\Delta p = 2.395$Pa (c) $\Delta p = 2.514$Pa

Figure 13: Centerline position case optimized result under different pressure drop constraint value. (a) and (c) are chosen by declining 5% and raising 5% than design (b)(case (1) in Figure 12).

Table 6: Results of designs in Fig. 13 under different pressure drop constraints

result	Objective functional	ϕ Darcy	ϕ_{post} RANS	Vol.	Δp Darcy
(a)$u_0 = 0.20$m/s	Reference design	4.72	14.72	0.56	2.39
$Re = 10,000$	optimized	2.63	5.33	0.56	2.28
(b)$u_0 = 0.20$m/s	Reference design	4.72	14.72	0.56	2.39
$Re = 10,000$	optimized	2.92	5.69	0.56	2.39
(c)$u_0 = 0.20$m/s	Reference design	4.720	14.72	0.56	2.39
$Re = 10,000$	optimized	2.97	7.37	0.56	2.51

process started with a uniform grey distribution and the volume constraint is set for $f = 0.56$. The verification results in Tab. 7 show that all the optimized results exhibit better cooling performances than the reference design, despite the simulation error between the full-blown model and the proposed equivalent model.

5. Conclusions

Topology optimized cooling channels are designed using a simplified approach based on a Darcy-flow based convective heat transfer model. Upon calibrating the parameters and material properties of this linear model, it serves as an efficient and viable alternative to a turbulent flow model for topology optimization. Importantly, the computational gain compared to a more accurate turbulent flow simulation is desirable at the early conceptual design stage, when the details of the channel features are unknown and performing a full-blown turbulent flow simulation is computationally too intensive. However, due to lack of the inertia term, the equivalent model cannot fully replace the RANS model when describing the turbulent flows and the actual temperature field. The optimization results hence still need verification by a turbulence model. Imposing a minimum length scale on the channel designs by geometrical constraints

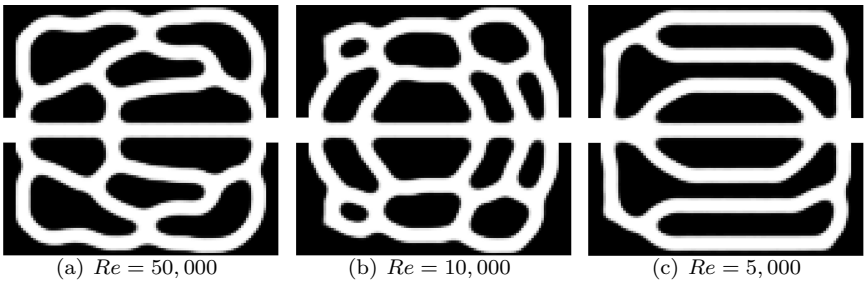

(a) $Re = 50,000$ (b) $Re = 10,000$ (c) $Re = 5,000$

Figure 14: Centerline position case optimized result under various Reynolds number that with velocity boundary condition (a)$u_0 = 1.00$m/s, (b)$u_0 = 0.20$m/s(design(1) in Fig. 12) and (c)$u_0 = 0.10$m/s.

Table 7: Results of designs in Fig. 14 under different Reynolds numbers

result	Objective functional	ϕ Darcy	ϕ_{post} RANS	Vol.	Δp Darcy
(a)$u_0 = 1.00$m/s	Reference design	2.02	6.65	0.56	11.88
$Re = 50,000$	optimized	1.67	2.40	0.56	11.88
(b)$u_0 = 0.20$m/s	Reference design	4.72	14.72	0.56	2.39
$Re = 10,000$	optimized	2.92	5.69	0.56	2.39
(c)$u_0 = 0.10$m/s	Reference design	8.83	20.16	0.56	1.12
$Re = 5,000$	optimized	3.51	8.32	0.56	1.12

is found important not only to ensure manufacturability but also to suppress intermediate densities during the optimization. The pressure drop constraint turns out to be necessary in obtaining energy-efficient and meaningful channel designs. Although the case study is initial-design dependent, the approach gives reasonable results with the proposed design strategies.

Acknowledgements

The authors acknowledge the financial support received from China Scholarship Council and from the research project "Sapere Aude TOpTEn" (Topology Optimization of Thermal ENergy systems) from the Danish Council for Independent Research, grant: DFF-4005-00320.

Appendix A. Sensitivity analysis

By help of the adjoint method [20], the objective functional is augmented by the product of adjoint fields and the residuals:

$$\hat{\phi} = \phi + \lambda_{\mathrm{t}}^{\mathrm{T}} \left(\left(\mathbf{K_t} + \mathbf{C}\left(\mathbf{p}\right) \right) \mathbf{t} - \mathbf{f_t} \right) + \lambda_{\mathrm{p}}^{\mathrm{T}} \left(\mathbf{K_p p} - \mathbf{f_p} \right), \tag{A.1}$$

where the convection term can be split such that the stabilization term is written separately, yielding:

$$\mathbf{C} = \mathbf{C}_1\left(\tilde{\boldsymbol{\xi}}, \mathbf{p}\right) + \mathbf{C}_{1\mathrm{uw}}\left(\tilde{\boldsymbol{\xi}}, \mathbf{p}, \mathbf{u}\left(\tilde{\boldsymbol{\xi}}, \mathbf{p}\right)\right), \tag{A.2}$$

with the expanding formulation are:

$$\mathbf{C}_1^e = \int_{\Omega^e} \rho c_p \mathbf{N}^{\mathrm{T}} \left(-\frac{\kappa}{\mu}\mathbf{B}\mathbf{p}^{\mathbf{e}}\right)^{\mathrm{T}} \mathbf{B}\mathrm{d}\Omega, \tag{A.3}$$

$$\mathbf{C}_{1\mathrm{uw}}^e = \int_{\Omega_e} \rho c_p \frac{\tilde{k}}{2}\mathbf{B}^{\mathrm{T}} \frac{\mathbf{u}}{\|\mathbf{u}\|}\mathbf{u}^{\mathrm{T}}\mathbf{B}\mathrm{d}\Omega, \tag{A.4}$$

then assembling to the global matrix getting $\mathbf{C}_1$ and $\mathbf{C}_{1\mathrm{uw}}$. The gradient of the Lagrangian function (A.1) is calculated by:

$$\begin{aligned}
\frac{\mathrm{d}\hat{\phi}}{\mathrm{d}\tilde{\boldsymbol{\xi}}} &= \frac{\partial\phi}{\partial\tilde{\boldsymbol{\xi}}} + \frac{\partial\phi}{\partial\mathbf{p}}\frac{\mathrm{d}\mathbf{p}}{\mathrm{d}\tilde{\boldsymbol{\xi}}} + \frac{\partial\phi}{\partial\mathbf{t}}\frac{\mathrm{d}\mathbf{t}}{\mathrm{d}\tilde{\boldsymbol{\xi}}} \\
&\quad + \lambda_{\mathrm{t}}^{\mathrm{T}}\left(\frac{\mathrm{d}\mathbf{K}_{\mathbf{t}}}{\mathrm{d}\tilde{\boldsymbol{\xi}}}\mathbf{t} + \frac{\partial\mathbf{C}}{\partial\tilde{\boldsymbol{\xi}}}\mathbf{t} + \frac{\partial\mathbf{C}}{\partial\mathbf{p}}\frac{\mathrm{d}\mathbf{p}}{\mathrm{d}\tilde{\boldsymbol{\xi}}}\mathbf{t} - \frac{\mathrm{d}\mathbf{f}_{\mathbf{t}}}{\mathrm{d}\tilde{\boldsymbol{\xi}}} + \left(\mathbf{K}_{\mathbf{t}} + \mathbf{C}\right)\frac{\mathrm{d}\mathbf{t}}{\mathrm{d}\tilde{\boldsymbol{\xi}}}\right) \\
&\quad + \lambda_{\mathrm{p}}^{\mathrm{T}}\left(\frac{\mathrm{d}\mathbf{K}_{\mathbf{p}}}{\mathrm{d}\tilde{\boldsymbol{\xi}}}\mathbf{p} - \frac{\mathrm{d}\mathbf{f}_{\mathbf{p}}}{\mathrm{d}\tilde{\boldsymbol{\xi}}} + \mathbf{K}_{\mathrm{p}}\frac{\mathrm{d}\mathbf{p}}{\mathrm{d}\tilde{\boldsymbol{\xi}}}\right),
\end{aligned} \tag{A.5}$$

where $\frac{\mathrm{d}\mathbf{f}_{\mathbf{t}}}{\mathrm{d}\tilde{\boldsymbol{\xi}}}$ and $\frac{\mathrm{d}\mathbf{f}_{\mathbf{p}}}{\mathrm{d}\tilde{\boldsymbol{\xi}}}$ are equal to zero due to the applied load not depending on the design variable. By collecting all the terms that contain the $\frac{\mathrm{d}\mathbf{t}}{\mathrm{d}\tilde{\boldsymbol{\xi}}}$ and $\frac{\mathrm{d}\mathbf{p}}{\mathrm{d}\tilde{\boldsymbol{\xi}}}$,$\lambda_{\mathrm{t}}$ and λ_{p} can be calculated as:

$$\lambda_{\mathrm{t}} = -\left(\mathbf{K}_{\mathbf{t}} + \mathbf{C}\right)^{-\mathrm{T}}\frac{\partial\phi}{\partial\mathbf{t}}, \tag{A.6}$$

$$\lambda_{\mathrm{p}} = -\mathbf{K}_{\mathbf{p}}{}^{-\mathrm{T}}\left(\frac{\partial\phi}{\partial\mathbf{p}} + \lambda_{\mathrm{t}}^{\mathrm{T}}\frac{\partial\mathbf{C}}{\partial\mathbf{p}}\mathbf{t}\right)^{\mathrm{T}}, \tag{A.7}$$

where

$$\frac{\partial\phi}{\partial\mathbf{t}} = \mathbf{L}^{\mathrm{T}}. \tag{A.8}$$

Here we need to notice that on boundary Γ_2, $T = 0$, so that $\frac{\partial\phi}{\partial\mathbf{t}} = 0$, and on boundary Γ_1, $p = 0$, so that $\frac{\partial\phi}{\partial\mathbf{p}} = 0$.The $\frac{\partial\mathbf{C}}{\partial\mathbf{p}}$ term contains the gradient of the convection term $\frac{\partial\mathbf{C}_1}{\partial\mathbf{p}}$ and stabilization term $\frac{\partial\mathbf{C}_{1\mathbf{uw}}}{\partial\mathbf{p}}$ which are discussed below. In the gradient formulation of objective functional the convection term is always multiplied with the temperature vector $\mathbf{t}$. Consider the gradient of their product

terms as:

$$\begin{aligned}\frac{\partial \mathbf{C}_1}{\partial \mathbf{p}^{\mathrm{e}}}\mathbf{t}^{\mathrm{e}} &= \frac{\partial}{\partial \mathbf{p}^{\mathrm{e}}}\left(\int_{\Omega_e} \rho c_p \mathbf{N}^{\mathrm{T}}\left(-\frac{\kappa}{\mu}\mathbf{B}\mathbf{p}^{\mathrm{e}}\right)^{\mathrm{T}}\mathbf{B}\mathrm{d}\Omega\right)\mathbf{t}^{\mathrm{e}} \\ &= \frac{\partial}{\partial \mathbf{p}^{\mathrm{e}}}\left(\int_{\Omega_e} \rho c_p \mathbf{N}^{\mathrm{T}}\left(-\frac{\kappa}{\mu}\mathbf{B}\mathbf{t}^{\mathrm{e}}\right)^{\mathrm{T}}\mathbf{B}\mathbf{p}^{\mathrm{e}}\mathrm{d}\Omega\right) \\ &= \int_{\Omega_e} \rho c_p \mathbf{N}^{\mathrm{T}}\left(-\frac{\kappa}{\mu}\mathbf{B}\mathbf{t}^{\mathrm{e}}\right)^{\mathrm{T}}\mathbf{B}\mathrm{d}\Omega = \mathbf{C}_{\mathbf{2}}^{\mathrm{e}}. \end{aligned} \tag{A.9}$$

Then multiply term $\frac{\mathrm{d}\mathbf{p}^{\mathrm{e}}}{\mathrm{d}\mathbf{p}}$, which is a $4\times N$ sparse matrix that only has 4 elements equal to 1, assembly formula (A.9) and can be written as

$$\frac{\partial \mathbf{C}_1}{\partial \mathbf{p}}\mathbf{t} = \mathbf{C}_2\left(\mathbf{t}\right). \tag{A.10}$$

The upwind term is a function of $\mathbf{u}$, the derivation with respect to $\mathbf{p}$ can be calculated from the element as:

$$\frac{\partial \mathbf{C}_{1uw}}{\partial \mathbf{p}^{\mathrm{e}}}\mathbf{t}^{\mathrm{e}} = \frac{\partial \mathbf{c}_{1uw}}{\partial \mathbf{u}^{\mathrm{e}}}\frac{\partial \mathbf{u}^{\mathrm{e}}}{\partial \mathbf{p}^{\mathrm{e}}}\mathbf{t}^{\mathrm{e}} \tag{A.11}$$

$$= \int_{\Omega_e} \frac{h_e}{2}\rho c_p \mathbf{B}^{\mathrm{T}}\frac{\partial}{\partial \mathbf{u}^{\mathrm{e}}}\left(\frac{\mathbf{u}^{\mathrm{e}}\mathbf{u}^{\mathrm{e}\mathrm{T}}}{\|\mathbf{u}^{\mathrm{e}}\|}\right)\frac{\partial \mathbf{u}^{\mathrm{e}}}{\partial \mathbf{p}^{\mathrm{e}}}\mathbf{B}\mathbf{t}^{\mathrm{e}}\mathrm{d}\Omega, \tag{A.12}$$

where the derivative term of velocity $\frac{\partial}{\partial \mathbf{u}^{\mathrm{e}}}\left(\frac{\mathbf{u}^{\mathrm{e}}\mathbf{u}^{\mathrm{e}\mathrm{T}}}{\|\mathbf{u}^{\mathrm{e}}\|}\right)$ can be calculated as two 4×4 matrices, multiplied with term $\frac{\partial \mathbf{u}^{\mathrm{e}}}{\partial \mathbf{p}^{\mathrm{e}}} = -\frac{\kappa}{\mu}\mathbf{B}$, which is a 2×4 matrix integrated on element. Then the same assembly and multiply process as the convective term, the formula (A.12) can be written as:

$$\frac{\partial \mathbf{C}_{1\mathrm{uw}}}{\partial \mathbf{p}}\mathbf{t} = \mathbf{C}_{2\mathrm{uw}}\left(\mathbf{t}\right). \tag{A.13}$$

And the term $\frac{\partial \mathbf{C}}{\partial \mathbf{p}}\mathbf{t}$ can be calculated as $\mathbf{C}_2 + \mathbf{C}_{2\mathrm{uw}}$. The sensitivity analysis result is compared with the finite difference result. The relative error in a 100×100 elements case is less than 0.5%. The rest sensitive analysis of filter, volume constraint and pressure drop constrain can be easily found in [23, 26, 3].

Reference

[1] Alexandersen, J., Aage, N., Andreasen, C.S., Sigmund, O.: Topology optimisation for natural convection problems. International Journal for Numerical Methods in Fluids **76**, 699–721 (2014). DOI 10.1002/fld.3954

[2] Alexandersen, J., Sigmund, O., Aage, N.: Large scale three-dimensional topology optimisation of heat sinks cooled by natural convection. International Journal of Heat and Mass Transfer **100**, 876–891 (2016). DOI 10.1016/j.ijheatmasstransfer.2016.05.013

[3] Andreasen, C.S., Gersborg, A.R., Sigmund, O.: Topology optimization of microfluidic mixers. International Journal for Numerical Methods in Fluids **61**, 498–513 (2009). DOI 10.1002/fld.1964

[4] Bendsøe, M.P., Kikuchi, N.: Generating optimal topologies in structural design using a homogenization method. Computer Methods in Applied Mechanics and Engineering **71(2)**, 197–224 (1988). DOI 10.1016/0045-7825(88)90086-2

[5] Bendsøe, M.P., Sigmund, O.: Topology optimization: Theory, methods and applications. Springer (2003)

[6] Borrvall, T., Petersson, J.: Topology optimization of fluids in stokes flow. International Journal for Numerical Methods in Fluids **41**, 77–107 (2003). DOI 10.1002/fld.426

[7] Brinkman, H.: A calculation of the viscous force exerted by a flowing fluid on a dense swarm of particles. Applied Scientific Research **A1 Issue 1**, 27–34 (1947). DOI 10.1007/BF02120313

[8] Brooks, A.N., Hughes, T.J.: Streamline upwind/petrov-galerkin formulations for convection dominated flows with particular emphasis on the incompressible navier-stokes equations. Computer Methods in Applied Mechanics and Engineering **32**, 119–259 (1982). DOI 10.1016/0045-7825(82)90071-8

[9] Chan, I.W., Pinfold, M., Kwong, C., Szeto, W.: A review of research, commercial software packages and patents on family mould layout design automation and optimisation. The International Journal of Advanced Manufacturing Technology **47**, 23–47 (2011). DOI 10.1007/s00170-011-3268-8

[10] Choi, J.H., Kim, J.S., Han, E.S., Park, H.P., Rhee, B.O.: Study on an optimized configuration of conformal cooling channel by branching law. Proceedings of the ASME 2014 12th Biennial Conference on Engineering Systems Design and Analysis(ESDA2014),Copenhagen, Denmark (2014). DOI 10.1115/esda2014-20431

[11] Dede, E.M.: Multiphysics optimization, synthesis, and application of jet impingement target surfaces. The 12th IEEE Intersociety Conference on Thermal and Thermomechanical Phenomena in Electronic Systems (ITHERM),Las Vegas,Las Vegas (2010). DOI 10.1109/itherm.2010.5501408

[12] Gersborg-Hansen, A., Sigmund, O., Haber, R.B.: Topology optimization of channel flow problems. Structural and Multidisciplinary Optimization **30**, 181–192 (2005). DOI 10.1007/s00158-004-0508-7

[13] Guest, J., Prevost, J., Belytschko, T.: Achieving minimum length scale in topology optimization using nodal design variables and projection functions. Int J Numer Methods Eng **61(2)**, 238–254 (2004). DOI 10.1002/nme.1064

[14] Guest, J.K., Asadpoure, A., Ha, S.H.: Eliminating beta-continuation from heaviside projection and density filter algorithms. Structural and Multidisciplinary Optimization **44**(4), 443–453 (2011)

[15] Guest, J.K., Prevost, J.H.: Topology optimizaiton of creeping fluid flows using a Darcy-Stokes finite element. Internal Journal for Numerical Methods in Engineering **66**, 461–484 (2006). DOI 10.1002/nme.1560

[16] Hu, P., He, B., Ying, L.: Numerical investigation on cooling performance of hot stamping tool with various channel designs. Applied Thermal Engineering **96**, 338–351 (2016). DOI 10.1016/j.applthermaleng.2015.10.154

[17] Jarrett, A., Kim, I.Y.: Design optimization of electric vehicle battery cooling plates for thermal performance. Journal of Power Sources **196**, 10,359–10,368 (2011). DOI 10.1016/j.jpowsour.2011.06.090

[18] Koga, A.A., Lopes, E.C.C., Nova, H.V., Silva, E.C.N.: Development of heat sink device by using topology optimization. International Journal of Heat and Mass Transfer **64**, 759–772 (2013). DOI 10.1016/j.ijheatmasstransfer.2013.05.007

[19] Lengiewicz, J., Wichrowski, M., Stupkiewicz, S.: Mixed formulation and finite element treatment of mass-conserving cavitation model. Tribology International **72**, 143–155 (2014). DOI 10.1016/j.triboint.2013.12.012

[20] Michaleris, P., A.Tortorelli, D., Vidal, C.A.: Tangent operators and design sensitivity formulations for transient non-linear coupled problems with applications to elastoplasticity. International Journal for Numerical Methods in Engineering **37**, 2471–2499 (1994). DOI 10.1002/nme.1620371408

[21] Qian, X., Sigmund, O.: Topological design of electromechanical actuators with robustness toward over- and under-etching. Computer Methods in Applied Mechanics and Engineering **253**, 237–251 (2013). DOI 10.1016/j.cma.2012.08.020

[22] Qiao, H.: A systematic computer-aided approach to cooling system optimal design in plastic injection molding. International Journal of Mechanical Sciences **48**, 430–439 (2006). DOI 10.1016/j.ijmecsci.2005.11.001

[23] Sigmund, O.: Morphology-based black and white filters for topology optimization. Structural and Multidisciplinary Optimization **33**, 401–424 (2007). DOI 10.1007/s00158-006-0087-x

[24] Svanberg, K.: The method of moving asymptotes:a new method for structural optimization. International Journal for Numerical Methods in Engineering **24**, 359–397 (1987). DOI 10.1002/nme.1620240207

[25] Tan, H.Y., R.Najafi, A., J.Pety, S., R.White, S., H.Geubelle, P.: Gradient-based design of actively-cooled microvascular composite panels. International Journal of Heat and Mass Transfer **103**, 594–606 (2016). DOI 10.1016/j.ijheatmasstransfer.2016.07.092

[26] Wang, F., Lazarov, B.S., Sigmund, O.: On projection methods convergence and robust formulations in topology optimization. Structural and Multidisciplinary Optimization **43**, 767–784 (2011). DOI 10.1007/s00158-010-0602-y

[27] Wang, G., Zhao, G., Li, H., Guan, Y.: Research on optimization design of the heating/cooling channels for rapid heat cycle molding based on response surface methodology and constrained particle swarm optimization. Expert Systems with Applications **38**, 6705–6719 (2011). DOI 10.1016/j.eswa.2010.11.063

[28] Yoon, G.H.: Topological design of heat dissipating structure with forced convective heat transfer. Journal of Mechanical Science and Technology **24**(6), 1225–1233 (2010). DOI 10.1007/s12206-010-0328-1

[29] Zhou, M., Alexandersen, J., Sigmund, O., Pedersen, C.: Industrial application of topology optimization for combined conductive and convective heat transfer problems. Structural and Multidisciplinary Optimization **54**, 1045–1060 (2016). DOI 10.1007/s00158-016-1433-2

[30] Zhou, M., Lazarov, B.S., Wang, F., Sigmund, O.: Minimum length scale in topology optimization by geometric constraints. Computer Methods in Applied Mechanics and Engineering **293**, 266–282 (2015). DOI 10.1016/j.cma.2015.05.003